

# Interferometric Phase Linking

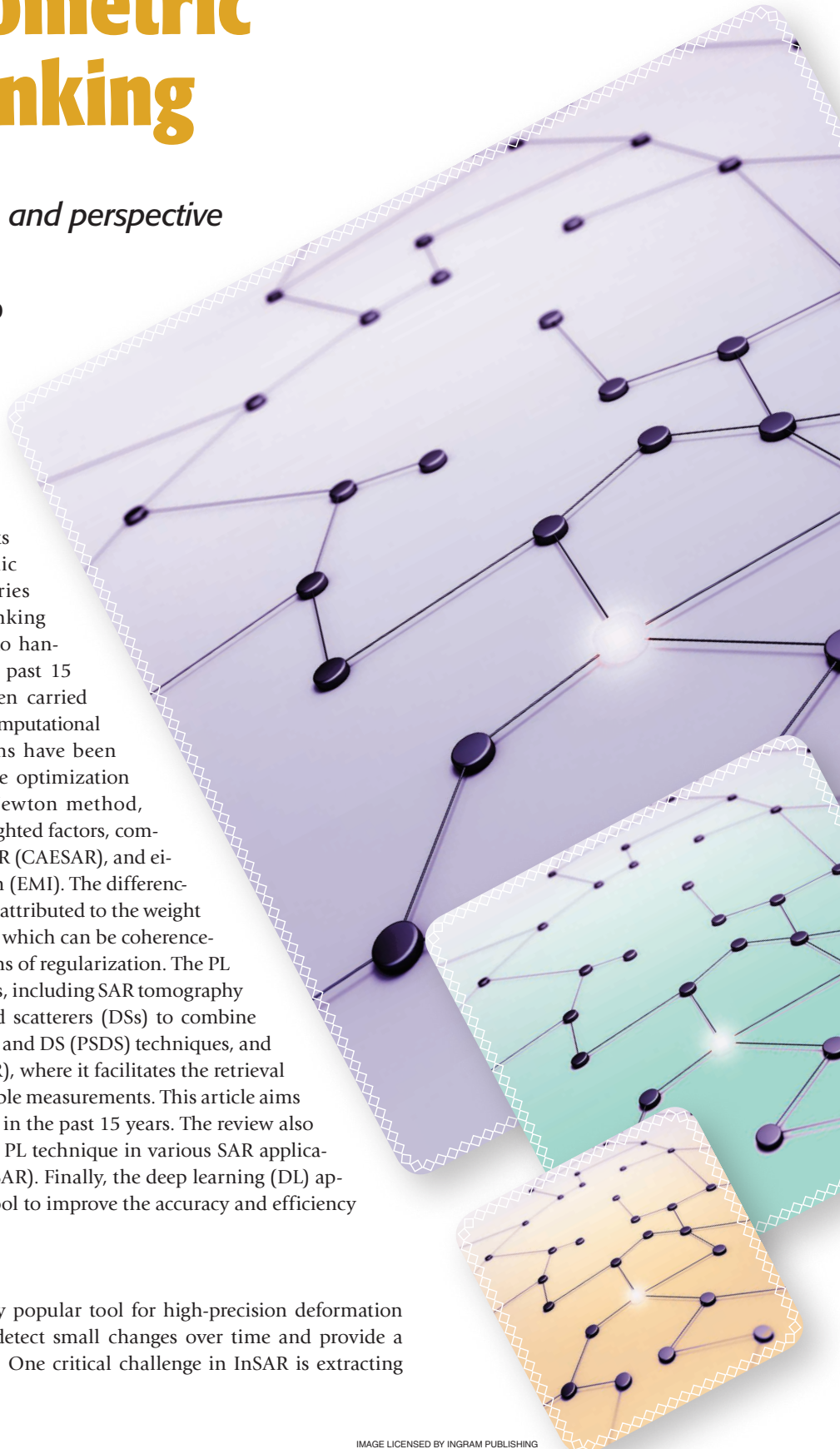
*Algorithm, application, and perspective*

DINH HO TONG MINH<sup>✉</sup> AND  
STEFANO TEBALDINI<sup>✉</sup>

Mitigating decorrelation effects on interferometric synthetic aperture radar (InSAR) time series data is challenging. The phase linking (PL) algorithm has been the key to handling signal decorrelations in the past 15 years. Numerous studies have been carried out to enhance its precision and computational efficiency. Different PL algorithms have been proposed, each with unique phase optimization approaches, such as the quasi-Newton method, equal-weighted and coherence-weighted factors, component extraction and selection SAR (CAESAR), and eigendecomposition-based algorithm (EMI). The differences among the PL algorithms can be attributed to the weight criteria adopted in each algorithm, which can be coherence-based, sparsity-based, or other forms of regularization. The PL algorithm has multiple applications, including SAR tomography (TomoSAR), enhancing distributed scatterers (DSs) to combine with persistent scatterers (PS) in PS and DS (PSDS) techniques, and compressed PSDS InSAR (ComSAR), where it facilitates the retrieval of the optimal phase from all possible measurements. This article aims to review PL techniques developed in the past 15 years. The review also underscores the importance of the PL technique in various SAR applications (TomoSAR, PSDS, and ComSAR). Finally, the deep learning (DL) approach is discussed as a valuable tool to improve the accuracy and efficiency of the PL process.

## INTRODUCTION

InSAR has become an increasingly popular tool for high-precision deformation monitoring, due to its ability to detect small changes over time and provide a unique view of Earth's surface [1]. One critical challenge in InSAR is extracting





meaningful information from the interferometric phase, which is affected by atmospheric conditions, topography, and decorrelations [2], [3]. Several techniques have been proposed to address these signal decorrelations to improve the interferometric phase's quality [1].

The first category of techniques is based on PS InSAR, which utilizes individual scatterers dominating the signal from a resolution cell to track deformation through time [4]. PS interferometry (PSI) techniques provide high-quality deformation information at point target locations.

However, in natural scenes, PSI technology, widely used for deformation estimation in urban areas, may not be sufficient to obtain accurate results, due to a low density of PSs [5]. To address the challenges associated with the limited information in InSAR data, an alternative approach is based on DSs, which offers the potential to leverage information more effectively. DS targets are commonly found in natural environments, such as meadows, fields, and bare soil, where multiple scatterers with similar brightness contribute to the information in a resolution cell. However, to account for signal decorrelation, one should select interferogram subsets for a temporal analysis using short spatial and temporal baselines, known as *small baseline subsets* (SBASs) [6], [7], [8]. This approach has demonstrated promising results in various applications, such as ground deformation monitoring and surface elevation mapping. The SBAS

approach offers a valuable alternative to traditional InSAR methods by leveraging the information from DSs [9]. However, deformation measurements on distributed targets are often of lower quality and require spatial multilooked filtering.

Another approach is the PL method introduced by Guarnieri and Tebaldini [10]. PL is defined as a statistical method used in interferometry to combine multiple interferometric phases into a single equivalent single-reference (ESR) phase. Suppose  $N$  single-look complex (SLC) images are available. The PL algorithm is the maximum likelihood estimation (MLE) of the  $N - 1$  ESR phase from all possible combinations of  $N(N - 1)/2$ . Before applying the SBAS approach, it is necessary to unwrap the interferograms. However, the PL method exploits all wrapped interferometric phases to optimize the phase quality. SqueeSAR technology [11], which uses a phase triangulation algorithm, is one example of the PL method. These optimized ESR phases of DS targets can be used in conventional PSI processing.

Accurately estimating linked phases is critical in coherent analysis for mitigating decorrelation effects on SAR data. Hence, numerous studies have been carried out to enhance the precision and computational efficiency of PL estimation since the work of Guarnieri and Tebaldini [10]. Ferretti et al. [11] proposed a quasi-Newton method for unconstrained nonlinear optimization, which is the Broyden–Fletcher–Goldfarb–Shanno algorithm [12] for the MLE solution. This optimization technique is efficient in minimizing the nonlinear cost function of the PL problem. Cao et al. [13] introduced equal-weighted and coherence-weighted factors for phase optimization, which provide flexibility for incorporating coherence information. The CAESAR algorithm [14] was proposed for phase optimization under multiple scattering mechanisms. It is based on the coherence matrix's eigenvalue decomposition (EVD) and can extract different scattering components. The EMI algorithm proposed by Ansari et al. [15] is also EVD based and MLE based. It is efficient in computation and estimation due to its exploitation of coherence information. Ho Tong Minh and Ngo [16] proposed a compression technique for PL estimation. The method involves dividing massive data into ministacks and then compressing them to enhance the noise-free short-lived interferometric components. Finally, Zwieback [17] proposed regulation methods to improve the estimation of the coherence matrix. The improvement in the compression [16] and regulation [17] approaches is most significant for low long-term coherences, due to more reliable coherence matrix estimates. Overall, the differences among the PL algorithms can be attributed to the weight criteria adopted in each algorithm, which can be coherence-based, sparsity-based, or other forms of regularization.

Addressing signal decorrelations to improve the interferometric phase's quality is crucial for many applications. The PL algorithm has been instrumental in handling this issue in the past 15 years. In the past five years, there have been 826 review articles published, while the total number of papers related to PL since its introduction is 1,286, according to results from Google Scholar as of June 2023. However, there is a need for a comprehensive review of the different PL algorithms proposed so far. Notably, no comprehensive review has been conducted thus far on the relationship between PL and its applications in diverse SAR methodologies, including TomoSAR, PSs and DSs, and the ComSAR algorithm. This article aims to bridge this knowledge gap by providing an overview of the PL techniques developed over the past 15 years and emphasizing the significance of the PL technique in various SAR applications. Furthermore, the potential of employing DL as a valuable tool to enhance the precision and efficiency of the PL process is explored and discussed. Table 1 provides nomenclature used throughout the article.

## PHASE LINKING MODELS AND PROPOSED ALGORITHMS

### CLOSURE PHASE PROBLEM

Suppose that  $N$  SLC SAR images are available for a specific area of interest. The images are coregistered on a reference grid, and phase contributions due to terrain topography and orbit have been compensated. Let  $\gamma_n$  be the  $n$ th coregistered SLC images in the form of

$$\gamma_n = S_n \exp(j\varphi_n) \quad (1)$$

where  $S_n$  is the amplitude and  $\varphi_n$  is the phase of  $\gamma_n$ . With three SAR images, it is possible to generate three single-look interferograms written as

$$\gamma_{12} = \gamma_1 \gamma_2^*, \quad \gamma_{13} = \gamma_1 \gamma_3^*, \quad \gamma_{23} = \gamma_2 \gamma_3^* \quad (2)$$

where  $*$  denotes the complex conjugate. The closure phase is the circular combination of the three interferometric phases:

$$\Psi_{1,2,3} = W \{ \varphi_{12} + \varphi_{23} + \varphi_{31} \} \quad (3)$$

where  $W$  is the wrapping (modulo- $2\pi$ ) operator,  $\varphi_{nm} = \varphi_n - \varphi_m$  is the single-look interferometric phase of  $\gamma_{nm}$ , and  $\varphi_{nm}$  includes contributions related to the residual

topography, deformation, atmosphere, and noise [2]. For single pixels, the closure phase  $\Psi_{1,2,3}$  is always zero by definition and is called the *phase consistency condition* or *phase triangularity condition* [18], [19]. However, the phase triangularity condition is not necessarily valid for multilooked interferometric pixels, as the closure phase can be nonzero [11], [19], [20]. Figure 1 shows an example of a full-scene closure phase from three multilooked interferometric phases. It has been derived from *Advanced Land Observing Satellite (ALOS) 2/Phased-Array L-Band Synthetic Aperture Radar (PALSAR) 2* data acquired over Vietnam. Ho Chi Minh City occupies the west center of the image.

Notably, it has been demonstrated that nonsymmetric volumetric targets have a nonzero phase closure [20]. This implies that the zero-closure model assumes no phase closure and is inadequate for volume scattering scenarios, such as forests and glaciers. In such cases, multilooked interferograms assume a mathematical model representing the volumetric target as an “equivalent point target” with a “phase center” position. Consistent with this interpretation, the mathematical model of multilooked interferograms assumed in PL algorithms is given as

$$E \{ \gamma_n \gamma_m^* \} = \gamma_{nm} \sigma_n \sigma_m \exp(j(\phi_n - \phi_m)) \quad (4)$$

where  $E$  denotes spatial averaging,  $\gamma_{nm}$  is the coherence of the  $nm$ th interferometric pair,  $\sigma_n = \sqrt{E \{ S_n^2 \}}$ ,  $\phi_n$  is the multilook interferometric phase for the  $n$ th acquisition, and  $\phi_{nm} = \phi_n - \phi_m$  is the multilook interferometric phase of  $\gamma_{nm}$ .

Equation (4) requires reevaluating the phase estimation in a stack of SAR images. The selection and weighting of the interferograms can affect the accuracy of the reconstructed

**TABLE 1. NOMENCLATURE USED IN THIS ARTICLE.**

ABBREVIATION	EXPANSION
CAESAR	Component extraction and selection synthetic aperture radar
CNN	Convolutional neural network
ComSAR	Compressed persistent scatterers and distributed scatterers interferometric SAR algorithm
DL	Deep learning
CRLB	Cramér Rao lower bound
DS	Distributed scatterer
EMI	Eigendecomposition-based maximum likelihood estimator of interferometric phase
ESA	European Space Agency
ESR	Equivalent single reference
EVD	Eigenvalue decomposition
GAN	Generative adversarial network
MLE	Maximum likelihood estimator
Insar	Interferometric SAR
PCA	Principal component analysis
PL	Phase linking
PS	Persistent scatterer
PSDS	PSs and DSS
PSI	PS interferometry
PU	Phase unwrapping
RNN	Recurrent NN
SAR	Synthetic aperture radar
SBAS	Small baseline subsets
SHP	Statistically homogeneous pixel
SLC	Single-look complex
TomoSAR	SAR tomography
TPSA	Two-stage programming approach

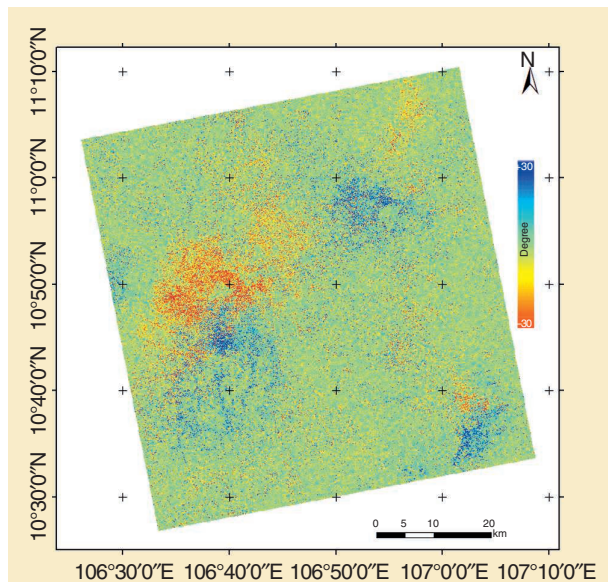


**FIGURE 1.** The closure phase corresponds to three *ALOS-2/PALSAR-2* acquisitions over Vietnam, acquired on 12 January, 23 March, and 10 August 2018. Ho Chi Minh City is recognizable in the west center of the image.

phase history. PL is a technique to address this statistical disclosure.

### COHERENCE MATRIX

Under the hypothesis of distributed scattering, the probability density function of the data may be regarded as a zero-mean multivariate circular normal distribution. Therefore, an ensemble of the second-order moments (i.e., a covariance matrix or a coherence matrix) represents sufficient statistics to infer information from the data. Compared to a covariance matrix, the coherence matrix can avoid amplitude disturbance among SAR images. For simplicity, we assume, without any loss of generality, that the images are normalized such that  $\sigma_n = 1$  for every  $n$  [see (4)] in the remainder of this article. Under this assumption, the covariance matrix is identical to a coherence matrix. The expression of a sampled coherence matrix can be defined as

$$\hat{\Gamma} = E[\mathbf{y}\mathbf{y}^H] \approx \frac{1}{L} \sum_{\mathbf{y} \in \Omega} \mathbf{y}\mathbf{y}^H \quad (5)$$

where  $H$  is the conjugate transpose and represents a homogeneous patch containing  $L$  adjacent pixels with similar scattering properties. The absolute and phase values of the elements of  $\hat{\Gamma}$  are the estimated coherence value  $\hat{\gamma}$  and interferometric phase  $\phi_n$ , respectively. Therefore,  $\hat{\Gamma}$  can be expressed as

$$\hat{\Gamma} = \begin{bmatrix} 1 & \hat{\gamma}_{12}e^{j\phi_{12}} & \dots & \hat{\gamma}_{1N}e^{j\phi_{1N}} \\ \hat{\gamma}_{21}e^{j\phi_{21}} & 1 & \dots & \hat{\gamma}_{2N}e^{j\phi_{2N}} \\ \vdots & \vdots & \ddots & \vdots \\ \hat{\gamma}_{N1}e^{j\phi_{N1}} & \hat{\gamma}_{N2}e^{j\phi_{N2}} & \dots & 1 \end{bmatrix} = |\hat{\Gamma}| \circ \Phi \quad (6)$$

where  $\Phi$  is an  $N \times N$  matrix, with element  $e^{j\phi_{nm}}$  indicating the interferometric phases between the  $n$ th acquisition and  $m$ th acquisition. In this case,  $\hat{\Gamma}$  represents an  $N \times N$  matrix with element  $\hat{\gamma}_{nm}$ .

### MAXIMUM LIKELIHOOD ESTIMATION

#### PHASE LINKING

Based on the central limit theorem, we assume that the normalized SAR data vector  $\mathbf{y}$  follows a complex multivariate normal distribution with zero mean and dispersion matrix  $\Sigma$ . The dispersion matrix  $\Sigma$  represents the scattering properties of a DS. Recalling  $\Sigma$  as a model for the underlying covariance of a complex circular Gaussian process, it is known that the probability density function of  $\hat{\Gamma}$  follows a complex Wishart distribution with  $L$  degrees of freedom [13]:

$$p(\hat{\Gamma} | \Sigma) = \frac{(L)^{NL} \det(\hat{\Gamma})^{L-N} \exp\{-\text{tr}[L\Sigma^{-1}\hat{\Gamma}]\}}{\pi^{\frac{N(N-1)}{2}} \det(\Sigma)^L \prod_{j=1}^N (\text{gamma}(L-j+1))} \quad (7)$$

where  $\text{tr}(\cdot)$  and  $\det(\cdot)$  indicate the trace and determinant operators. The  $\Sigma$  of a generic pixel can be expressed using "true" coherence values and "true" phase values as

$$\Sigma = \Theta G \Theta^H \quad (8)$$

where

$$\Theta = \begin{bmatrix} e^{j\vartheta_1} & 0 & \dots & 0 \\ 0 & e^{j\vartheta_2} & \dots & 0 \\ \vdots & \vdots & \ddots & \vdots \\ 0 & 0 & \dots & e^{j\vartheta_N} \end{bmatrix}$$

$$G = \begin{bmatrix} 1 & \gamma_{12} & \dots & \gamma_{1N} \\ \gamma_{21} & 1 & \dots & \gamma_{2N} \\ \vdots & \vdots & \ddots & \vdots \\ \gamma_{N1} & \gamma_{N2} & \dots & 1 \end{bmatrix}.$$

Here,  $\lambda = [\vartheta_1, \vartheta_2, \dots, \vartheta_N]^T$  is the optimal phase that needs to be estimated from the filtered  $N(N-1)/2$  phases. It should be noted that the  $N(N-1)/2$  interferometric phase values are not redundant, due to the spatial filtering process. Furthermore, the estimation of the absolute phase series is ambiguous. The phase of an arbitrary image in the time series is set to zero, and the remaining values are measured comparably to this arbitrary datum. Without any loss of generality, the first value can be set to zero, such as  $\lambda = [0, \vartheta_2, \dots, \vartheta_N]^T$ . Therefore, only  $N - 1$  phase values need to be estimated. PL is a technique to estimate the optimal  $N - 1$  interferometric phases from the possible  $N(N-1)/2$  phases. In other words, PL can be understood as combining multiple interferometric phases into an ESR phase. PL is commonly formulated as an optimization problem.

Given  $\hat{\Gamma}$  obtained from (5), the MLE of  $\Sigma$  follows from the maximization of the Wishart probability density function given by

$$\hat{\Sigma} = \underset{\Sigma}{\operatorname{argmax}} \left\{ \ln[p(\hat{\Gamma} | \Sigma)] \right\} \\ = \underset{\Sigma}{\operatorname{argmax}} \left\{ -\text{tr}(\Sigma^{-1}\hat{\Gamma}) - L \ln(\det(\Sigma)) \right\} \\ = \underset{G, \Theta}{\operatorname{argmin}} \left\{ \text{tr}(\Theta G^{-1} \Theta^H \hat{\Gamma}) + \ln(\det(G)) \right\}. \quad (9)$$

To estimate  $\Theta$ , the true coherence  $G$  is required. Since  $G$  is unknown in practice, it is common to use the standard plug-in estimate by setting it as

$$G = |\hat{\Gamma}| \quad (10)$$

resulting in unregularized PL and guaranteeing nonnegativeness [17]. We then can write (9) as

$$\hat{\Sigma} = \underset{\Theta}{\operatorname{argmin}} \left\{ \text{tr}(\Theta | \hat{\Gamma} |^{-1} \Theta^H \hat{\Gamma}) \right\}. \quad (11)$$

Equation (11) was originally proposed by Guarnieri and Tebaldini [10]. To ensure a unified analysis, considering the variations in PL approaches, (11) can be reformulated based on the employed weighting strategy. In detail, at row  $n$  and column  $m$ , the MLE of the phase value is [13]

$$\hat{\lambda}_{MLE} = \underset{\lambda}{\operatorname{argmin}} \left\{ \sum_{n=1}^N \sum_{m=n+1}^N \gamma'_{nm} \cos(\phi_{nm} - \vartheta_n + \vartheta_m) \right\} \quad (12)$$

where  $\gamma'_{nm}$  is the element of Hadamard product  $|\hat{\Gamma}|^{-1} \circ \hat{\Gamma}$ , defined as the weight factor in the optimization, and  $\circ$  represents the Hadamard entry-wise product. In practice, a damping factor is used in the algorithm to remove small negative or null eigenvalues of the matrix  $|\hat{\Gamma}|$  before matrix inversion. The MLE may be interpreted as a temporal filter that compresses the information of  $N(N-1)/2$  interferograms to a phase series of size  $N$ . The solution of (12) is achieved by iteratively minimizing [10]. After this procedure, the DS phase values are filtered, resulting in more reliable PU. With this assumed

### ONE CRITICAL CHALLENGE IN INSAR IS EXTRACTING MEANINGFUL INFORMATION FROM THE INTERFEROMETRIC PHASE, WHICH IS AFFECTED BY ATMOSPHERIC CONDITIONS, TOPOGRAPHY, AND DECORRELATIONS.

model, the scattering behavior of the DS neighborhood is approximated by a PS-resembling mechanism.

### RECENT ADVANCES

Estimating the linked phase is the crucial step in coherent analysis to account for decorrelating targets. Consequently, dedicated research focuses on improving the precision and computational efficiency in the work of Guarnieri and Tebaldini [10]. These techniques can be categorized into two main groups. The first approach is based on computation methods involving optimization, iteration, or EVD [11],

[13], [14], [15]. On the other hand, the second approach involves estimating the coherence matrix, which can be achieved through regularization or compression techniques [16], [17].

Ferretti et al. [11] proposed a quasi-Newton method for unconstrained nonlinear optimization, i.e., the Broyden–Fletcher–Goldfarb–Shanno algorithm [12], for the MLE solution. Cao et al. [13] introduced equal-weighted and coherence-weighted factors in the phase optimization. They proposed a modified MLE algorithm incorporating the coherence matrix. The coherence-weighted algorithm can be more accurate than the equal-weighted one in temporal decorrelation. Fornaro et al. [14] proposed a specific CAESAR algorithm for estimating the phase in the presence of multiple scattering mechanisms. The authors used an EVD-based approach to extract different scattering components from the coherence matrix. The algorithm was shown to be accurate and computationally efficient for estimating the phase in the presence of multiple scattering mechanisms. Ansari et al. [15] proposed an EVD-based MLE (EMI) algorithm to estimate the phase. They used an EVD approach to reduce the problem's dimensionality and improve the algorithm's computational efficiency. The initial solution can be found as the minimum eigenvector of the matrix  $|\hat{\Gamma}|^{-1} \circ \hat{\Gamma}$ . Ho Tong Minh and Ngo [16] proposed a data compression technique to improve the precision of the phase estimation algorithm. The authors divided massive data into many ministacks and then compressed them. The improvement of the phase estimation algorithm from the compression is due to the noise-free short-lived interferometric components. Zwieback [17] proposed a method for improving the estimation of the coherence matrix by regulating the coherence matrix estimates. For instance, with spectral regularization,  $\hat{\Gamma}_{\text{regularization}} = \beta I + (1 - \beta) \hat{\Gamma}$ , with  $\beta$  varied from zero to one. The regularization techniques impose constraints

TABLE 2. CHARACTERISTICS OF THE MAIN PL APPROACHES.

METHOD/ REFERENCE	NAME	WEIGHT	DESCRIPTION
<b>COMPUTATION</b>			
Guarnieri and Tebaldini [10]	MLE	$\gamma'_{nm}$	The element of Hadamard product $ \hat{\Gamma} ^{-1} \circ \hat{\Gamma}$ , with the iterative solution
Ferretti et al. [11]	MLE	$\gamma'_{nm}$	Similar to Guarnieri and Tebaldini [10], with the solution by the Broyden–Fletcher–Goldfarb–Shanno algorithm
Cao et al. [13]	Coherence	$\hat{\gamma}_{nm}$	The element of coherence matrix $\hat{\Gamma}$ (with equal-weighted factor $\hat{\gamma}_{nm} = 1$ )
Fornaro et al. [14]	EVD	$\hat{\gamma}_{nm} \gamma'_{nm}$	$\gamma'_{nm}$ is the element of matrix $ \gamma   \gamma ^T$ , where $ \gamma $ is the maximum eigenvector of coherence matrix $\hat{\Gamma}$
Ansari et al. [15]	EMI	$\gamma'_{nm}$	Similar to Guarnieri and Tebaldini [10], with the iterative solution that initializes as the minimum eigenvector of the matrix $ \hat{\Gamma} ^{-1} \circ \hat{\Gamma}$
<b>COHERENCE MATRIX</b>			
Ho Tong Minh and Ngo [16]	MLE	$\gamma_{nm}^{\text{compression}}$	The element of Hadamard product $ \hat{\Gamma}_{\text{compression}} ^{-1} \circ \hat{\Gamma}_{\text{compression}}$
Zwieback [17]	MLE	$\gamma_{nm}^{\text{regularization}}$	The element of Hadamard product $ \hat{\Gamma}_{\text{regularization}} ^{-1} \circ \hat{\Gamma}_{\text{regularization}}$

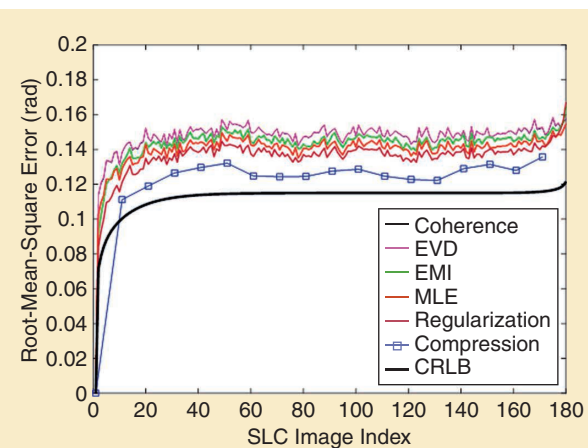


FIGURE 2. PL performances using a Sentinel-1 temporal coherence model. The coherence is modeled as two exponential decays and a long-term coherent component [21], [16]. The performances are ordered to facilitate the visualization.

on the coherence matrix estimates to improve their accuracy. In compression [16] and regularization [17] approaches, the improvements are most significant for low long-term coherences, due to more reliable coherence matrix  $\hat{\Gamma}$  estimates. In summary, the difference among the PL algorithms can be interpreted as the adopted weight criteria, as in (12). Table 2 gives the characteristics of different PL approaches.

Figure 2 illustrates PL performances. We employ a well-documented coherence Sentinel-1 model to simulate the behavior of temporal coherence over time [21], [16]. This model generates a coherence matrix for a three-year time series of 180 temporally ordered measurements taken at six-day intervals. Each measurement includes an ensemble of 300 statistically homogeneous samples. The simulation is repeated 1,000 times. The EMI solution corresponds to the minimum eigenvector of the matrix  $|\hat{\Gamma}|^{-1} \circ \hat{\Gamma}$ . The spectral regularization is used with a  $\beta$  of 0.5. We set the ministack as 10 for the compression method. The CRLB is a theoretical measure that employs simulated coherence for the calculation, as described in [10]. The EVD and coherence weight results are very similar. The compressed estimator performs better than other approaches, closely approximating the CRLB. The compressed estimator's reduced error is attributed to the lack of noise in short-lived components [16].

It is essential to highlight that the significance of PL becomes more pronounced in ill-posed InSAR scenarios. However, with specific well-posed InSAR techniques, such as the TSPA, PU methods are already integrated into the processing workflow [22]. Thus, exploring the synergy between PL and the TSPA could lead to exciting research opportunities and further advancements in handling challenging InSAR scenarios.

Since the introduction of PL, there have been numerous SAR applications. Among them, the PSDS technique has gained immense popularity, as it surpasses PSI in terms of performance [11]. In tomographic focusing, the PL algorithm plays a crucial role in the phase calibration, as it requires an optimal phase model to compensate for potential phase residuals that may affect 3D imaging [23]. The ComSAR technique is a recent advancement that utilizes PL algorithms to select the most coherent interferograms based on their linked phases [16]. These applications are discussed in the "Applications" section.

## APPLICATIONS

### SYNTHETIC APERTURE RADAR TOMOGRAPHY

TomoSAR is a relatively new technique that has emerged as a powerful tool for the 3D imaging of complex scenes [24]. TomoSAR builds upon the capability of SAR systems to acquire data from multiple angles, which enables the reconstruction of the 3D structure of the imaged object [25]. In the case of forests, TomoSAR can be used to retrieve the vertical distribution of scatterers within the canopy, providing

valuable information on forest structure [26], [27], classification [28], and biomass [23].

Conventional SAR imaging of forests is challenging due to the complex interaction between the radar signal and forest canopy. The forest canopy is composed of vegetation layers that attenuate and scatter the radar signal in a complex way, making it difficult to retrieve information on the underlying terrain and vegetation [23]. TomoSAR can overcome some of these limitations by exploiting the 3D structure of the forest.

When the radar's wavelength is long enough to penetrate the forest canopy, it becomes possible to use multiple SAR acquisitions with slightly different look angles over the same area to quantify the three dimensions of forest reflectivity. This principle is demonstrated in Figure 3(a) and (c), where acquisitions from traditional SAR and TomoSAR are shown, respectively.

**PL IS DEFINED AS A STATISTICAL METHOD USED IN INTERFEROMETRY TO COMBINE MULTIPLE INTERFEROMETRIC PHASES INTO A SINGLE EQUIVALENT SINGLE-REFERENCE PHASE.**

To further elaborate on the TomoSAR process, consider a scenario where a sensor carefully flies along  $N$  parallel tracks and acquires multibaseline data of SAR images. Each pixel at the slant range  $r$  and azimuth location  $x$  in the  $n$ th image is denoted by  $y_n(r, x)$ . The azimuth axis  $x$  is defined by the direction of the aircraft platform, whereas the slant range  $r$  is the distance line of sight (LOS) linking the SAR's sensor to targets on the ground, as in Figure 3(c). It is assumed that each image within the multibaseline dataset has been coregistered and resampled on a common grid (i.e., the reference track) and that phase components due to terrain topography and platform motion have been compensated. Thus, the multibaseline SAR model can be written as [24], [23]

$$y_n(r, x) = \int S(\xi, r, x) \exp\left(j \frac{4\pi}{\lambda r} b_n \xi\right) d\xi \quad (13)$$

where  $\xi$  is the cross-range coordinate, defined by the direction orthogonal to the LOS and azimuth coordinate;  $b_n$  is the normal baseline relative to the  $n$ th image with respect to the reference image;  $\lambda$  is the carrier wavelength; and  $S(\xi, r, x)$  is the average scene complex reflectivity within the slant range, azimuth, and cross-range resolution cell, as described in Figure 3(d).

It is worth noting that the SAR scene and its geometric configuration are linked. Specifically, the distribution of the SAR scene's reflectivity in the cross-range direction is directly related to the multibaseline SAR data. These two components form a Fourier pair [as shown in (13)]. As a result, it is possible to reconstruct the cross-range distribution of the scene's complex reflectivity by taking the Fourier transform, as follows [23]:

$$\hat{S}(\xi, r, x) = \sum_{n=1}^N y_n(r, x) \exp\left(-j \frac{4\pi}{\lambda r} b_n \xi\right). \quad (14)$$

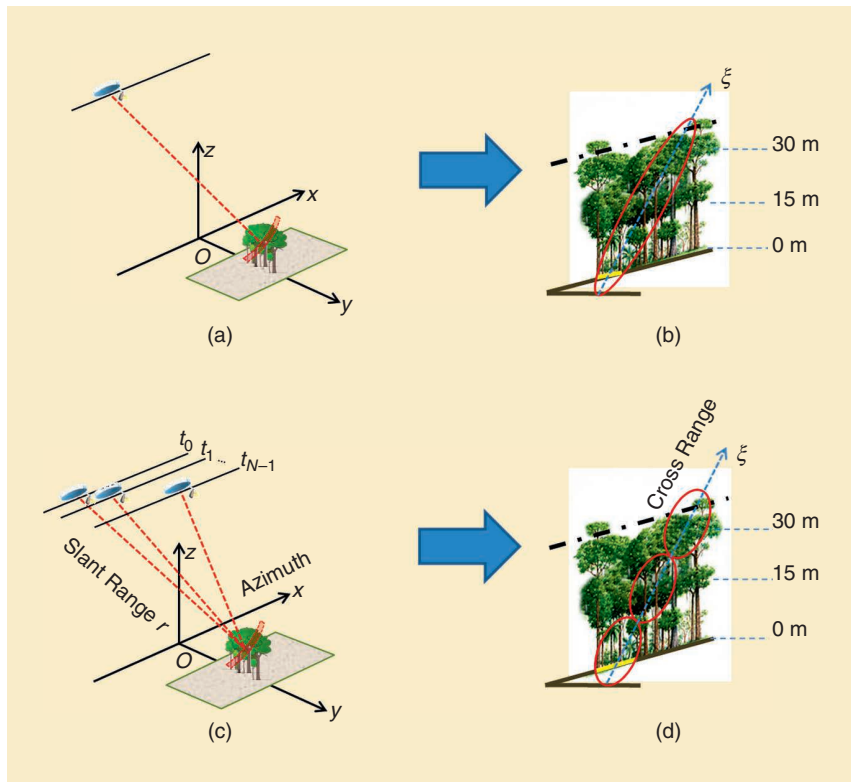


**FIGURE 3.** A comparison of traditional SAR and TomoSAR acquisitions. (a) and (b): Traits of traditional SAR. (c) and (d): Traits of TomoSAR. (a) A SAR acquisition. (b) A SAR resolution cell. (c) A TomoSAR acquisition. (d) A TomoSAR resolution cell. The figure was adapted from [29, Fig. 2].

Consequently, TomoSAR processing enables us to obtain the cross-range distribution of the SAR scene's reflectivity at every range and azimuth location. By doing so, we can obtain a 3D image that provides comprehensive information on the reflectivity of a forest in three dimensions. This information can be used to derive valuable forest structure characteristics, such as height and biomass [23], [29], [30].

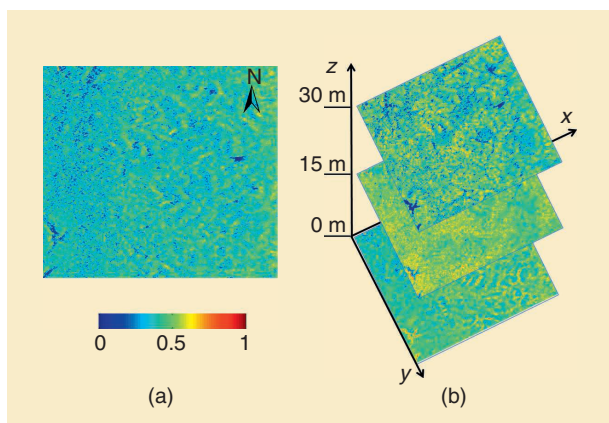


**FIGURE 4.** A comparison of traditional SAR and TomoSAR imaging. (a) A traditional SAR image from the Paracou, French Guiana, forest site. (b) TomoSAR layers, with each related to a certain height above the ground. The figure was adapted from [29, Fig. 4(b)].

Tomographic analysis relies on the outline theoretical model that assumes a disturbance-free propagating signal. Before focusing, a phase calibration procedure is required to compensate for phase residuals potentially affecting 3D focusing [20], [31], [32]. In addition, analyzing the backscattered power from different heights in a forest makes it possible to gain insight into the scattering mechanisms within the canopy [23]. To successfully implement this concept, a vertical axis reference must be established, which enables height measurements with respect to terrain elevation. The ground surface is often called the "zero-meter layer." However, the ground phase contribution must be separated from the vegetation phase to prevent it from influencing the 3D focusing.

These two points can be made by removing the ground phase contribution in the tomographic data [23]. The ground phases are determined not only by terrain height  $z_g$  but also by the phase disturbances  $\eta$  deriving from the platform motion.

In a formula,  $\varphi_{\text{ground}} = k_z z_g + \eta$ , where  $k_z = 4\pi b_n / \lambda \sin \theta R_n$  is the height-to-phase factor and  $\theta$  is the local incidence angle. The multipolarimetric multibaseline covariance matrix  $W$  can be approximated by retaining the first two terms of the sum of the Kronecker products [33]. In a formula,  $W \approx C_G \otimes R_G + C_V \otimes R_V$ , where  $R$  and  $C$  are referred to as *interferometric information* and *polarimetric information*, respectively, and  $G$  and  $V$  are associated with ground-only and volume-only contributions, respectively. PL is a fundamental component in facilitating the retrieval of this ground phase contribution from  $R_G$ . Indeed, applying PL to forested areas allows for representing forest scattering in terms of the "equivalent point target," with well-defined distances from the radar in different trajectories. This allows for simultaneous target and radar position estimation, after which platform motion can be corrected with subwavelength accuracy [20]. Figure 4 presents an example of SAR and TomoSAR imaging in the Paracou tropical forest site (French Guiana, South America).

#### PERSISTENT SCATTERERS AND DISTRIBUTED SCATTERERS TECHNIQUE

The PSDS technique is an approach that leverages the phase change over time of both PS and DS targets [1]. The technique involves two main steps: 1) PL and signal decorrelation removal and 2) estimation of parameters of interest. PSDS refers to techniques that exploit the time series phase

change of both PS and DS targets. SqueezSAR technology [11] is one example of the PSDS technique.

The PL technique is applied first to all the  $N(N - 1)/2$  interferograms available from  $N$  images. It jointly exploits these interferograms to squeeze the best estimates of  $N - 1$  interferometric phases. Once the estimate of the  $N - 1$  linked phases has been produced, the second step is necessary to remove the signal decorrelations and estimate the parameters of interest, such as the elevation error and constant velocity, similar to the PS interferometry processing algorithm [1]. The PSDS technique is widely used in InSAR applications, as it provides a reliable way to detect and monitor changes in Earth's surface [34], [35], [36], [37]. It allows for detecting small and slow surface movements over a large area, which is helpful in surface deformation applications [38]. An example of how interferogram networks can be exploited in the InSAR time series techniques is provided in Figure 5. The figure was generated using Constellation of Small Satellites for Mediterranean Basin Observation data over the Ha Noi, Vietnam, area. It illustrates how interferogram networks can be exploited to analyze PSDS targets over time [39].

It is important to note that PSI can be considered a particular case of the maximum likelihood interferometry approach [1]. In PSI, all PS targets are assumed to be equally correlated in all images. This assumption obviates the need for the joint processing of all available interferograms to estimate interferometric phase information. Instead, only removing the reference phase from all other phases is necessary to obtain the linked phases required for estimating parameters, such as surface deformation. The PSDS algorithm is an extension of the PSI method that considers both PS and DS targets. The joint processing of all available interferograms in PSDS can help account for variations in the radar signal caused by different surface characteristics, including changes in moisture content, surface roughness, and vegetation cover. As a result, the PSDS approach can offer greater accuracy and detail than the PSI method in detecting and measuring surface deformation.

The DS target is known for its low average temporal coherence, primarily due to geometrical and temporal decorrelation phenomena [3]. As a result, this target often has a low signal-to-noise ratio, making it challenging to work with. However, enhancing the DS target's signal-to-noise ratio and treating it as a PS target is possible by identifying pixels within a neighborhood that exhibit similar behavior. These similar pixels are called SHPs. They can be identified using a two-sample Kolmogorov-Smirnov [11] or Baumgartner-Weiss-Schindler [40] test on the amplitude-based time series of the current pixel and its neighbors within a specified window. The pixels with a similar cumulative probability distribution are grouped as "brothers," resulting in a family of SHPs [see Figure 6(a)]. A DS candidate is identified if it has a sufficient number of SHPs

that exceed a certain threshold [16]. Once a DS candidate is identified, its sample coherence matrix can be computed using its SHP family. The coherence matrix fully characterizes the target statistics and can be used to invert for  $N - 1$  linked phases using PL.

The quality of the estimated  $N - 1$  phase values can be assessed using the PL coherence, defined as [11]

$$\gamma_{PL} = \frac{2}{N(N-1)} \operatorname{Re} \sum_{n=1}^N \sum_{m=n+1}^N \exp(i(\phi_{nm} - \vartheta_n + \vartheta_m)). \quad (15)$$

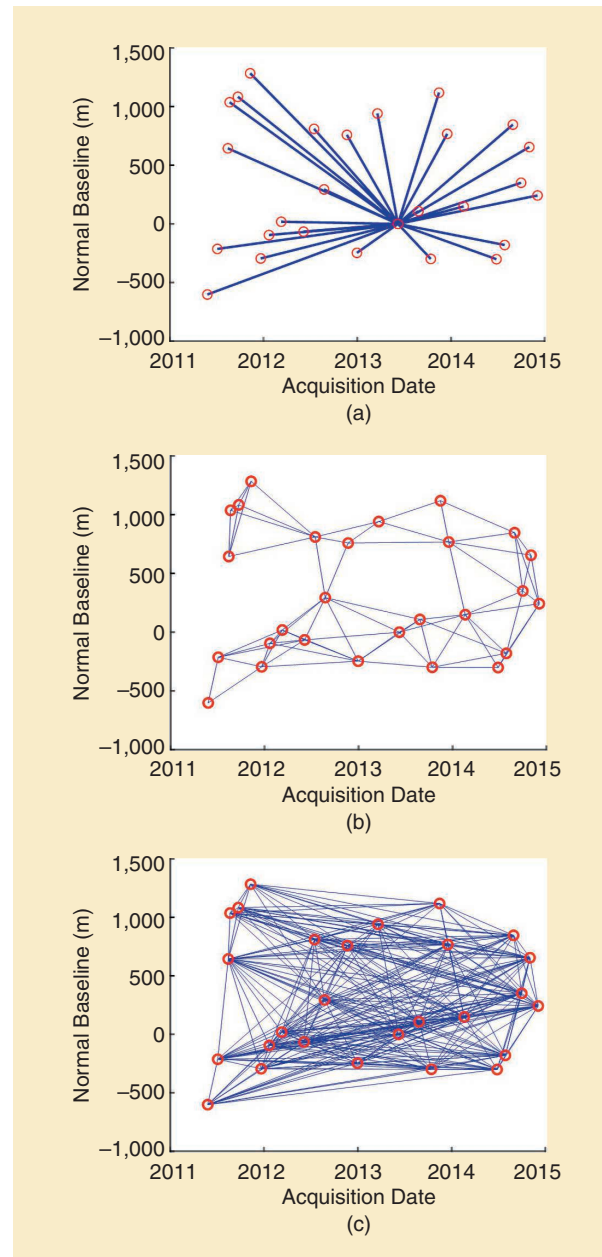


**FIGURE 5.** Interferogram networks. (a) The single master network in PSI processing. (b) The subset network consists of interferograms with short spatial and temporal baselines in SBASs. (c) The fully connected network in the PSDS technique.

If the  $\gamma_{PL}$  coherence is above a certain threshold, a DS point with the linked  $N - 1$  phase value will replace the original points. Finally, the selected DS will jointly process

using the same PSI technique as the PS. Figure 6(b) is an example of PL coherence, which is in full resolution, allowing for more comprehensive PL performance.

Improving PL and selecting SHPs are critical aspects of PSDS techniques. Various modified approaches have been proposed to select SHPs, including the Anderson–Darling test [34], time series likelihood ratios [41],

t-test [42], fast SHP selection, Baumgartner–Weiss–Schindler test [40], mean amplitude difference [43], and similar time series interferometric phase [44], among others. These approaches aim to increase the density of DSs, mitigating sample coherence bias. Additionally, the conventional DS assumption of independent

small scatterers with a uniform scattering mechanism can be relaxed by considering DS targets dominated by two or more scattering mechanisms [36], [45]. Engelbrecht et al. [45] showed that incorporating multiple scattering mechanisms in L-band ALOS PALSAR data improved deformation measurement extraction in dynamic agricultural regions. Recently, it has been demonstrated that adding polarimetric information can increase the number of coherent pixels by a factor of eight compared to a single-polarization channel [46]. Overall, improving SHP selection and PL, as well as considering more complex scattering mechanisms, can enhance the performance of PSDS techniques in deformation monitoring and other applications.

### COMPRESSED PERSISTENT SCATTERERS AND DISTRIBUTED SCATTERERS INTERFEROMETRIC SYNTHETIC APERTURE RADAR TECHNIQUE

The recent trend of spaceborne SAR missions focuses on systematic Earth monitoring with high temporal resolution [47], [48]. This has resulted in unprecedented SAR data volumes due to short revisit cycles, as brief as six to 12 days, with missions such as the ESA's Sentinel-1 [49] and NASA–Indian Space Research Organization Synthetic Aperture Radar mission [50]. However, interferometric processing of these large data stacks with currently available algorithms is infeasible. To address this demand, efforts have focused on reducing product latency through parallelized computation and cloud computing. One of the first efficient stacking techniques that allows for efficient PL in sequences using isolated data batches of the time series is the sequential estimator [51]. The ComSAR algorithm introduced by Ho Tong Minh and Ngo [16] has been proposed for processing PSDS analysis. Since most deformation phenomena develop slowly, a processing scheme can be devised using reduced-volume data sets. The algorithm divides massive data into many ministacks and compresses them.

Conventional MLE PL suffers from a high computational time complexity driven by the number of SLCs involved, primarily due to the iterative maximum likelihood optimization for the phase estimation and secondarily due to the regularization and inversion of the complex coherence matrix, both of which are affected by the number of interferograms. To address the high-data-volume problem, data compression is a classic approach in dealing with high data volumes. In the case of multi-pass SAR, the objective is to compress a stack of coregistered SAR data in the temporal direction so that the size of the time series is reduced but the spatial size of each image is intact. To perform data compression, PCA is a well-known technique [52], [53]. However, PCA fails to incorporate the statistical properties of the complex covariance matrix data correctly, as it is a geometrical rather than a probabilistic approach [53]. On the other hand, MLE PL is a purely probabilistic approach and is well

**EXPLORING THE SYNERGY BETWEEN PL AND THE TSPA COULD LEAD TO EXCITING RESEARCH OPPORTUNITIES AND FURTHER ADVANCEMENTS IN HANDLING CHALLENGING INSAR SCENARIOS.**

t-test [42], fast SHP selection, Baumgartner–Weiss–Schindler test [40], mean amplitude difference [43], and similar time series interferometric phase [44], among others. These approaches aim to increase the density of DSs, mitigating sample coherence bias. Additionally, the conventional DS assumption of independent

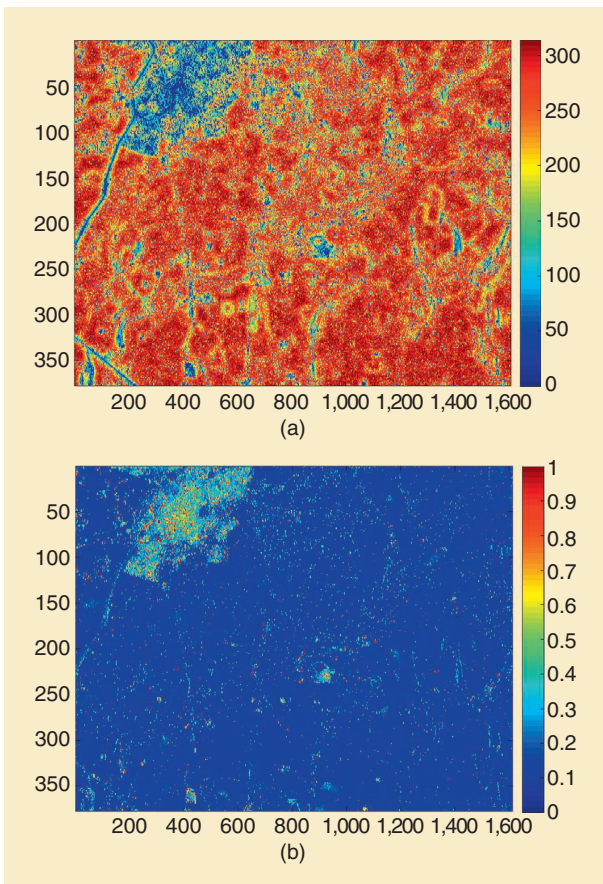


**FIGURE 6.** Internal results from PSDS-based processing. (a) The number of SHPs was identified using the Baumgartner–Weiss–Schindler test on a  $9 \times 35$  window. (b) The PL coherence corresponds to the SHP map. The figure was adapted from [16, Fig. 4].

known for its precise phase estimation [10], [51]. Therefore, the simple idea is to use the most coherent interferograms from their linked phases because the linked phases are optimal from all possible interferometric phases. This approach reduces the data volume by using the most informative interferograms for further processing, thereby allowing for efficient interferometric processing.

Let us assume that the  $N$  SAR dataset (ordered temporally) can be divided into small batches, or ministacks, with  $M$  images. The compressed version  $\hat{S}$  of  $M$  SAR images for the  $k$ th sequence can be determined by a coherent summation, as follows [51], [16]:

$$\hat{S}(r, x) = \sum_{m=1}^M S_m(r, x) \zeta_m \quad (16)$$

where  $\zeta = \hat{\Lambda}/\|\hat{\Lambda}\| = [\xi_1, \xi_2, \dots, \xi_M]$ .  $\hat{\Lambda} = \exp(j\hat{\lambda}^k)$  is the linked phase from  $M$  SAR images and  $S(r, x)$  is the scene complex-valued SLC at the slant range azimuth position. The vector  $\zeta$  weights each image's contribution in the ministack in the coherent summation process.

For each ministack, its compression is formed using (16), resulting in a strong data reduction. As an example of the algorithm's efficiency, from a stack of 90 images, we

can set  $M$  as 10 (see Figure 7). The processing will then estimate the 10 optimum phases by using the PL technique in (12). These phases allow us to coherently focus the stack subset and produce a single compressed image that can represent the 10 first images of the stack. The same procedure will be repeated on the following 10 images until the end of the stack, producing nine compressed images. We note that this process has to be performed on an SHP family basis since PL estimation can be valid only locally.

The ComSAR scheme in signal processing has benefits beyond just reducing the computational burden. It also prevents the need for updating and re-estimating the entire phase history at the face of every single acquisition. The processing scheme reduces the data volume from the entire stack to the compressed SLCs, making storage easier. These compressed images can then be used as a reference point to link history ministacks with recent acquisitions and reconstruct the full phase time series [see Figure 7(d)]. In detail, PL will be performed on the compressed components ( $\hat{S}$ ), producing a vector  $\hat{\lambda}_{\text{cal}} = [\hat{\vartheta}_{\text{cal}}(1), \hat{\vartheta}_{\text{cal}}(2), \dots, \hat{\vartheta}_{\text{cal}}(K)]$  that contains the calibration phases for connecting the ministacks. The datum connection for the  $k$ th sequence is then carried out by [16]

$$\hat{\lambda}_{\text{unified}}^k = \hat{\lambda}^k + \hat{\vartheta}_{\text{cal}}(k) \quad (17)$$

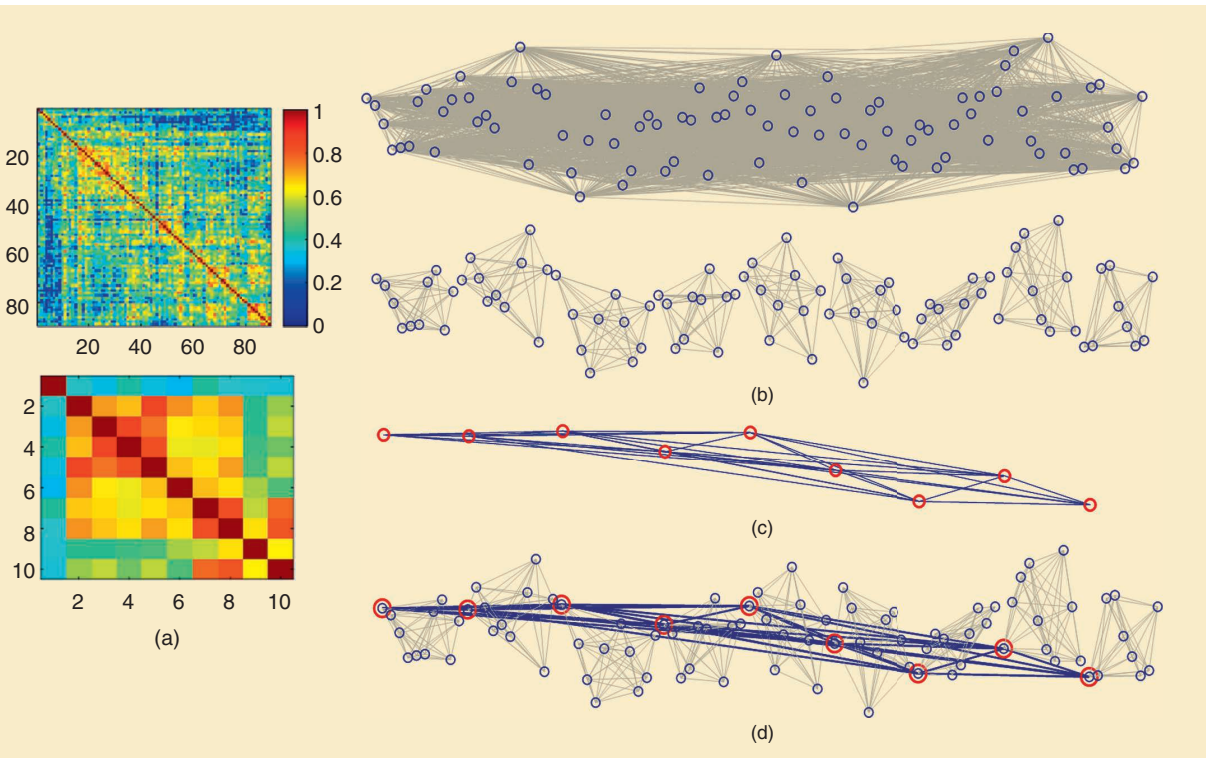


**FIGURE 7.** The ComSAR algorithm. (a) A full coherence matrix in the PSDS technique. The data are divided into ministacks with 10 images to improve the process efficiency. (b) The PL technique is employed to compress each ministack. This generates linked phases that enable a coherent focus on the stack subset, resulting in a compressed image representing the first 10 images. This compression procedure is repeated on the following 10 images, creating nine compressed images. These compressed images can be utilized to link prior ministacks with new acquisitions and reconstruct the full phase time series without the need to recalculate everything. ComSAR can work with full and compressed time series, but the (c) compressed version typically outperforms the (d) full time series version [16].

where the superscripts indicate the time series sequence and  $\hat{\theta}_{\text{cal}}(k)$  is the  $k$ th of the calibration vector.

Figure 8(a) displays an original interferogram covering 670 days in Mexico City, Mexico, while Figure 8(b) is a compressed version (with  $M = 10$ ). Compared to the original [in Figure 8(d) and (e)], the compressed interferogram exhibits superior quality and coherence. The average coherence improves from 0.4 to 0.8 [shown in Figure 8(c)], mainly because the noise component of the data is reduced in the compression process. Essentially, the noisy short-lived components are eliminated from the artificially compressed interferograms created from the ministacks. Consequently, these interferograms have a higher signal-to-noise ratio than the initial ones.

Since the estimation of the linked phase is ambiguous, we set the phase of the first image in each ministack to zero. Finally, PS values at these multireference images will be extracted from the original SLCs and integrated into compressed phase time series for PSDS analysis [16].

An interesting development by Ho Tong Minh and Ngo is the implementation of the PSDS and ComSAR algorithms, which have been made available as an open

source TomoSAR package [16], [54], [56]. To the best of our knowledge, this package is the first publicly accessible tool that enables the simultaneous handling of both PS and DS targets (<https://github.com/DinhHoTongMinh/TomoSAR>).

## PERSPECTIVE WITH DEEP LEARNING

This section highlights the potential of the DL approach in SAR data, emphasizing the value of DL in enhancing the accuracy and efficiency of PL. The “Brief Review of Deep Learning for Synthetic Aperture Radar Data” section serves as a bridge, introducing DL’s potential for SAR data processing and paving the way for its application in improving PL techniques, in the “Perspective for Phase Linking” section.

## BRIEF REVIEW OF DEEP LEARNING FOR SYNTHETIC APERTURE RADAR DATA

In recent years, the increase in SAR Earth observation missions, such as TerraSar-X, Sentinel-1, ALOS, and RADARSAT, has led to a new scenario characterized by the continuous generation of a massive amount of data. On the one hand, this trend has allowed us to observe the inadequacy

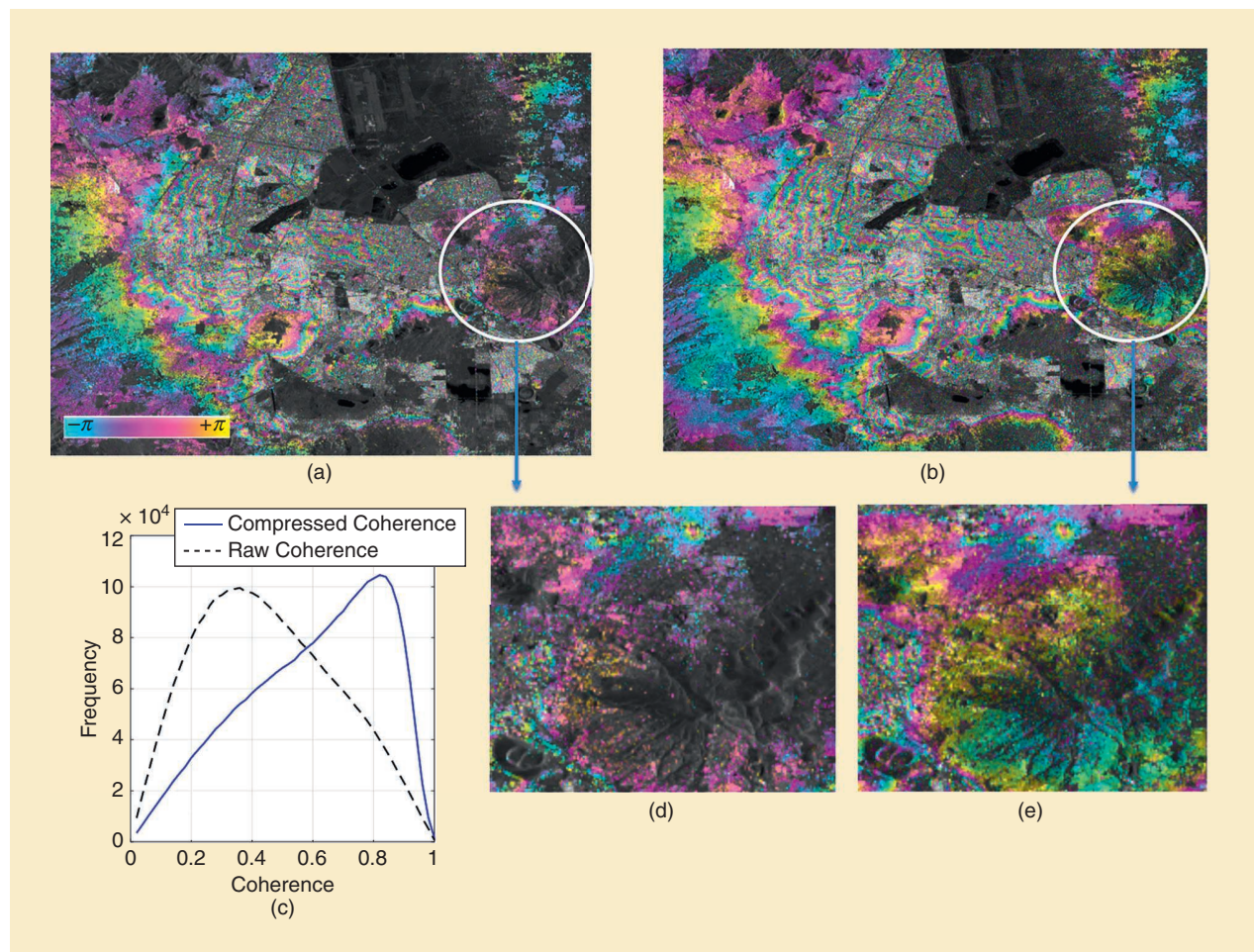


**FIGURE 8.** Mexico interferograms. (a) A raw 670-day interferogram. (b) A compressed 670-day interferogram. (c) The coherence distribution. (d) and (e) Zoomed-in versions of (a) and (b), respectively. The figure is adapted from [54, Fig. 3].

of classical algorithms in regard to generalization capabilities and computational performance; on the other hand, it paved the way for the new artificial intelligence paradigm, including the DL approach [57]. DL has profoundly impacted many scientific fields, such as machine vision, natural language processing, video processing, speech, image processing, and Earth data science [58], [59]. Over the past decade, significant advances have been made in developing and applying DL techniques to problems in Earth observation [59], [60], [61]. These techniques have proved highly effective for classification and parameter retrieval tasks, as they can process large amounts of data and deal efficiently with complex spatial and temporal structures [59]. DL has been applied to the field of SAR imaging. CNNs, GANs, and RNNs are the leading neuron network DL architectures that have been applied to SAR data analysis. CNNs have been widely used in various tasks, such as ship detection [62], building detection [63], deformation observation [64], and land cover classification [61], [65], and they have shown to be effective in these tasks. On the other hand, GANs have been used for SAR image super-resolution and to enhance the quality of SAR images [66]. RNNs have been applied to classify time series SAR data and have shown good results [60], [67].

Several studies have explored DL approaches for SAR filtering with promising results. For instance, Mullissa et al. [68] proposed a deSpeckNet DL-based approach for SAR despeckling that achieved higher accuracy and efficiency than traditional methods. Similarly, Wu et al. [69] used a deep CNN for polarimetric SAR filtering and demonstrated improved filtering performance. Promising outcomes have been achieved by exploring DL techniques in SAR PU tasks. Traditional PU methods assume that the phase possesses spatial continuity, but their effectiveness is hampered by decorrelation noise and aliasing fringes that invalidate such assumptions. To enhance the reliability of unwrapping outcomes, Wu et al. [70] proposed a deep CNN, known as a *discontinuity estimation network*, that predicts the probabilities of phase discontinuities in interferograms. Similarly, Zhou et al. [71] converted the PU problem into a learnable image semantic segmentation problem and presented a DL-based branch cut deployment approach (BCNet). Experimental results demonstrate that the proposed BCNet-based PU method is a near-real-time PU algorithm with higher accuracy than traditional PU methods. Accurate identification of PSs is crucial in obtaining reliable phase information in PSI and PSDS. To address this, a novel deep CNN named PSNet has been proposed by Tianxiang et al. [72] for PS identification. The significant advantage of PSNet lies in its deep architecture, which can learn the distinguishing features of PSs from vast training images with diverse topography and landscapes. Using the combined feature images of the average amplitude, amplitude dispersion, and coherence of interferograms as inputs, PSNet was trained to classify PS and non-PS pixels. The results demonstrate that PSNet accurately distinguishes between PS and non-PS

pixels. Notably, PSNet outperformed the StaMPS algorithm by detecting more than double the number of PSs.

### PERSPECTIVE FOR PHASE LINKING

The traditional PL methods rely on handcrafted algorithms, which can be time-consuming and may not always provide optimal results. DL has the potential to revolutionize the PL process in SAR imaging by providing an end-to-end solution that can learn the complex relationships between the interferometric phases and the ESR phase from data. The principle is quite simple for DL, which consists of multiple layers of interconnected nodes [58], [59], [73]. The general DL for PL can include the first

layer of the network extracting low-level features from the input data, such as the interferometric phases. The subsequent layers learn increasingly complex data representations until the final layer produces the desired output, such as the ESR phase. Unfortunately, we cannot find any report on the DL approach for the PL technique in the literature. For this reason, we discuss the possibility of DL as a valuable tool for PL by addressing a few selected points:

- Multipass SAR data are typically represented as complex-valued time series, which cannot be directly used as input to most DL models. One common approach is to separate the real and imaginary components and treat them as separate input channels. Alternatively, derived quantities, such as magnitude and phase, can be input. In both ways, the topographic phase must be subtracted to improve the spatial stationarity in the homogeneous region before feeding in the DL model [16]. Specialized NN architectures that handle complex-valued data directly, such as complex CNNs, also exist [74]. In addressing the PL problem, examining the data input approach is essential. Although few algorithms leverage the complex-valued nature of radar data [75], [76], separating the real and imaginary components or using magnitude and phase quantities as input are commonly used and practical approaches.
- One advanced CNN model is U-Net, an encoder-decoder CNN initially employed for semantic segmentation in medical images [77]. For example, a U-Net model could be trained to take SAR interferograms as input and output unwrapped phase maps, using significant annotated phase and deformation maps datasets [78]. This approach could improve the accuracy of the PU process and make it more robust to noise and other sources of error. Similarly, an autoencoder architecture is designed to effectively separate ground deformation signals from noise in InSAR time series without requiring any prior information about the location of a fault or its slip

**TRADITIONAL PL METHODS  
RELY ON HANDCRAFTED  
ALGORITHMS, WHICH CAN  
BE TIME-CONSUMING AND  
MAY NOT ALWAYS PROVIDE  
OPTIMAL RESULTS.**

behavior [64]. Indeed, U-Net is an architecture designed to learn a model in an end-to-end setting. U-Net's encoder path compresses the input image information by extrapolating relevant features computed at different resolution scales. As a result, this hierarchical feature extraction provides various representations of abstraction levels. On the other hand, U-Net's decoder path reconstructs the original image by mapping the intermediate representation back to the input spatial resolution. In particular, during this reconstruction process, the information is restored at different resolutions by stacking many upsampling layers. This can preserve relevant information during the decoding stage [77]. In this way, the reconstructed image accuracy can be well preserved. In this sense, there is a potential link between CNN U-Net models and PL.

- DL training can be performed by providing a large dataset of SAR images and their corresponding ESR phases. The network will use these data to learn the relationships between the interferometric phases and the ESR

phase, and it can then generalize these relationships to new SAR images. The DL approach's end-to-end nature means that a deep NN can perform the entire PL process, from feature extraction to ESR phase estimation. This results in a faster and more accurate PL process, as the network can automatically learn the most relevant features and relationships from the data [59], [73].

Exploiting DL for PL can bring two benefits. The first advantage is that it can handle nonstationary phase noise and outliers more effectively than traditional methods. Traditional PL methods rely on handcrafted algorithms, which may not always be robust to nonstationary phase noise and outliers. On the other hand, DL can learn to handle these issues from the data during the training process [79], resulting in a more robust PL process. Another advantage is a reduction of the computational cost of the process. Traditional PL methods can be computationally expensive, especially with large SAR datasets. DL, however, can be implemented on parallel architectures, such as GPUs, which can significantly reduce the

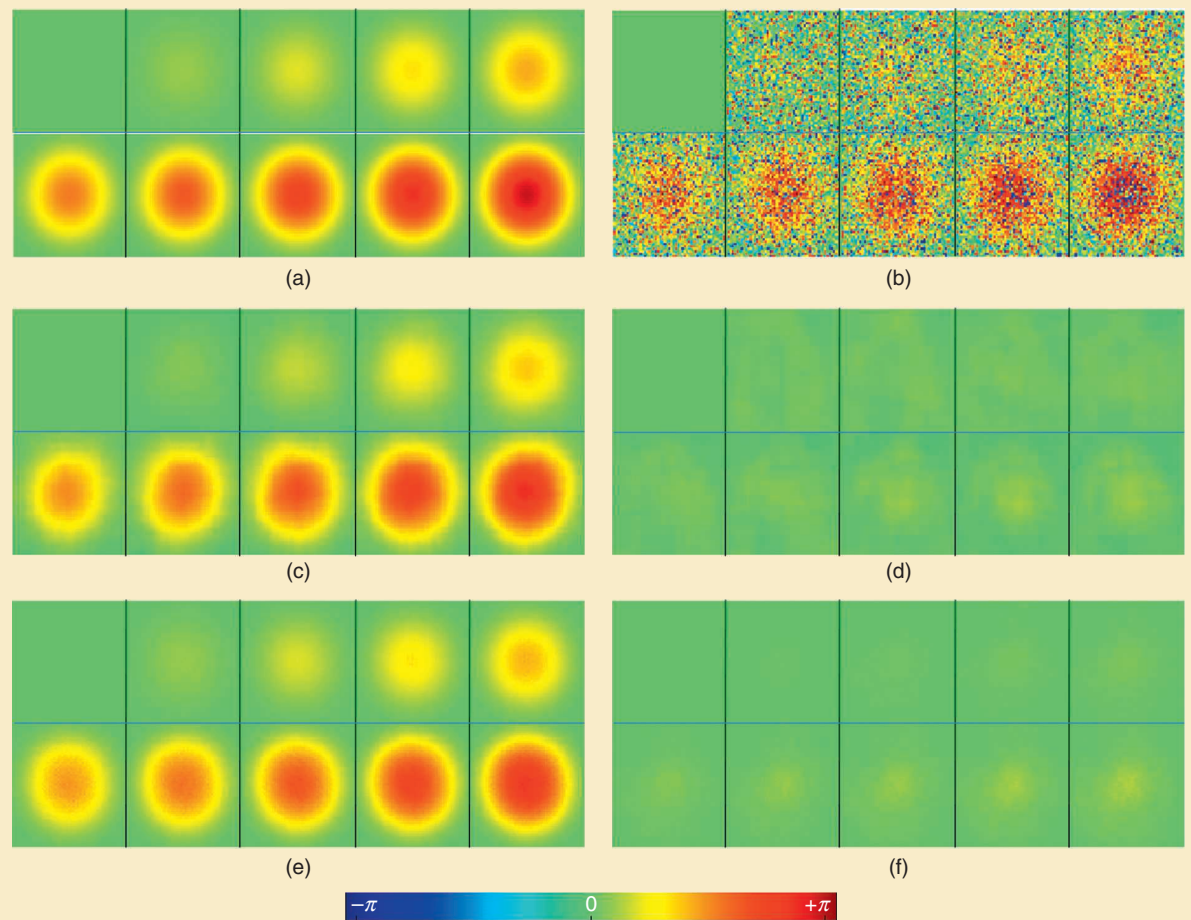


**FIGURE 9.** A synthetic example of PL using DL. (a) A simulated deformed signal for interferograms, using the first acquisition as the reference image. (b) Interferograms after adding decorrelation noise. (c) The results of the MLE method using all the interferograms. (d) The residuals of the MLE method [i.e., the difference between (a) and (c)]. (e) The results of the DL method using the U-Net model. (f) The residuals of the DL method [i.e., the difference between (a) and (e)].

computational cost [55]. This is particularly important for near-real-time processing of big SAR data, where the computational cost of the PL process is a significant concern.

In summary, DL holds considerable promise for various applications in PL, offering opportunities to enhance precision estimation and computational efficiency. Nevertheless, it is important to acknowledge the challenges and limitations associated with its implementation. These include data quality, feature extraction, model complexity, and interpretability concerns. While DL presents an enticing avenue for future research trends in PL, it necessitates a meticulous design and thorough evaluation of both the models and the data involved.

### EXAMPLE WITH U-NET MODEL

To demonstrate the applicability of DL in PL, we conducted a proof-of-concept test on a synthetic dataset. The simulation settings included generating a radar data stack with temporal noise behaviors, consisting of 10 SLC images with a revisit time of 35 days. We simulated a deformation signal by assuming a simple Gaussian deformation bowl with a maximum LOS deformation rate of 14 mm/year at the center and a radius of 600 m. The simulation was conducted on a flat area, resulting in a zero topographic signal. We assumed a crop of  $1,280 \times 1,280$  m, a radar wavelength of 56 mm, and a pixel size of  $20 \times 20$  m. We employed the coherence Sentinel-1 model to simulate the behavior of temporal coherence over time, which generates a coherence matrix for a one-year time series of 10 temporally ordered measurements taken at 35-day intervals [21], [16]. Each SLC included  $64 \times 64$  homogeneous pixels, and the simulation was repeated 5,000 times for DL data training. Figure 9(a) and (b) provides a visual representation of both the noise-free and noisy simulated datasets. Figure 9(c) and (d) demonstrates the application of the MLE spectral regularization algorithm using coherence matrix estimation over  $11 \times 11$  windows and a  $\beta$  value of 0.5 (see the “Recent Advances” section).

We used a MATLAB function called `unetLayers` to define the U-Net architecture, with a depth of three in the encoder network. The complex-valued interferometric data were separated by magnitude and phase quantities as input for the U-Net model, resulting in only  $2N - 1$  channels since the first phase is zero. The patch size was specified as  $64 \times 64 \times 19$ , and the number of output channels was nine ESR phases. We modified the U-Net architecture by replacing the original softmax layer with a regression layer and trained the model on a dataset of 4,800, measurements with 200 for validation, setting MaxEpochs as 10. Figure 9(e) and (f) indicates that the DL approach is expected to be comparable to the handcrafted MLE algorithm. However, it is important to note that the synthetic simulation used in this example was relatively basic. For future studies to effectively address the PL challenge using DL, it is crucial to have access to high-quality datasets containing both synthetic and real-world interferometric

patch images from various landscapes. Additionally, utilizing a more advanced U-Net model with greater depth can significantly enhance the accuracy and efficiency of the PL process.

### CONCLUSIONS

Accurate estimation of linked phases is crucial in mitigating decorrelation effects on SAR data in the PL technique. Researchers have proposed various algorithms, such as quasi-Newton, CAESAR, and EMI, to improve PL estimation’s precision and computational efficiency. Additionally, new compression and regulation techniques have been developed to enhance the estimation of the coherence matrix. PL is widely used in TomoSAR, PSDS, and ComSAR applications, and the adoption of DL is expected to improve the accuracy and efficiency of the process. The future of the DL approach for PL is promising, as ongoing research in various areas can shape the development of better algorithms and techniques. This will help improve the detection and measurement of surface deformation and parameter estimation in SAR applications, leading to more accurate and efficient results.

### ACKNOWLEDGMENT

This work was supported, in part, by the ESA; Center National d’Etudes Spatiales/Terre, Ocean, Surfaces Continentales, Atmosphere (project MekongInSAR); UMR TETIS; and Institut National de Recherche en Agriculture, Alimentation, et Environnement. The ALOS-2/PALSAR-2 data were kindly provided by the Japanese Aerospace Exploration Agency, under the third Research Announcement Program on Earth Observation, with project ER3A2N097.

### AUTHOR INFORMATION

**Dinh Ho Tong Minh** (dinh.ho-tong-minh@inrae.fr) is with UMR TETIS, INRAE, University of Montpellier, 34090 Montpellier, France. He is a Member of IEEE.

**Stefano Tebaldini** (stefano.tebaldini@polimi.it) is with Dipartimento di Elettronica, Informazione, e Bioingegneria, Politecnico di Milano, 20133 Milano, Italy. He is a Senior Member of IEEE.

### REFERENCES

- [1] D. Ho Tong Minh, R. Hanssen, and F. Rocca, “Radar interferometry: 20 years of development in time series techniques and future perspectives,” *Remote Sens.*, vol. 12, no. 9, Apr. 2020, Art. no. 1364, doi: 10.3390/rs12091364. [Online]. Available: <https://www.mdpi.com/2072-4292/12/9/1364>
- [2] R. F. Hanssen, *Radar Interferometry: Data Interpretation and Error Analysis*. Dordrecht, The Netherlands: Kluwer, 2001.
- [3] H. A. Zebker and J. Villasenor, “Decorrelation in interferometric radar echoes,” *IEEE Trans. Geosci. Remote Sens.*, vol. 30, no. 5, pp. 950–959, Sep. 1992, doi: 10.1109/36.175330.
- [4] A. Ferretti, C. Prati, and F. Rocca, “Permanent scatterers in SAR interferometry,” *IEEE Trans. Geosci. Remote Sens.*, vol. 39, no. 1, pp. 8–20, Jan. 2001, doi: 10.1109/36.898661.

- [5] A. Hooper, H. Zebker, P. Segall, and B. Kampes, "A new method for measuring deformation on volcanoes and other natural terrains using InSAR persistent scatterers," *Geophysical Res. Lett.*, vol. 31, no. 23, pp. 1–5, Dec. 2004, doi: 10.1029/2004GL021737.
- [6] P. Berardino, G. Fornaro, R. Lanari, and E. Sansosti, "A new algorithm for surface deformation monitoring based on small baseline differential SAR interferograms," *IEEE Trans. Geosci. Remote Sens.*, vol. 40, no. 11, pp. 2375–2383, Dec. 2002, doi: 10.1109/TGRS.2002.803792.
- [7] M.-P. Doin et al., "Presentation of the small baseline NSBAS processing chain on a case example: The Etna deformation monitoring from 2003 to 2010 using Envisat data," in *Proc. Fringe ESA Conf. Workshop*, Frascati, Italy, 2011, pp. 1–8.
- [8] Z. Yunjun, H. Fattah, and F. Amelung, "Small baseline InSAR time series analysis: Unwrapping error correction and noise reduction," *Comput. Geosci.*, vol. 133, Dec. 2019, Art. no. 104331, doi: 10.1016/j.cageo.2019.104331. [Online]. Available: <http://www.sciencedirect.com/science/article/pii/S0098300419304194>
- [9] D. Ho Tong Minh, R. Hanssen, M.-P. Doin, and E. Pathier, *Advanced Methods for Time-Series InSAR*. Hoboken, NJ, USA: Wiley, 2022, ch. 5, pp. 125–153.
- [10] A. M. Guarneri and S. Tebaldini, "On the exploitation of target statistics for SAR interferometry applications," *IEEE Trans. Geosci. Remote Sens.*, vol. 46, no. 11, pp. 3436–3443, Nov. 2008, doi: 10.1109/TGRS.2008.2001756.
- [11] A. Ferretti, A. Fumagalli, F. Novali, C. Prati, F. Rocca, and A. Rucci, "A new algorithm for processing interferometric data-stacks: SqueeSAR," *IEEE Trans. Geosci. Remote Sens.*, vol. 49, no. 9, pp. 3460–3470, Sep. 2011, doi: 10.1109/TGRS.2011.2124465.
- [12] R. Battiti and F. Masulli, *BFGS Optimization for Faster and Automated Supervised Learning*. Dordrecht, The Netherlands: Springer Netherlands, 1990, pp. 757–760.
- [13] N. Cao, H. Lee, and H. C. Jung, "Mathematical framework for phase-triangulation algorithms in distributed-scatterer interferometry," *IEEE Geosci. Remote Sens. Lett.*, vol. 12, no. 9, pp. 1838–1842, Sep. 2015, doi: 10.1109/LGRS.2015.2430752.
- [14] G. Fornaro, S. Verde, D. Reale, and A. Pauciuillo, "Caesar: An approach based on covariance matrix decomposition to improve multibaseline-multitemporal interferometric SAR processing," *IEEE Trans. Geosci. Remote Sens.*, vol. 53, no. 4, pp. 2050–2065, Apr. 2015, doi: 10.1109/TGRS.2014.2352853.
- [15] H. Ansari, F. De Zan, and R. Bamler, "Efficient phase estimation for interferogram stacks," *IEEE Trans. Geosci. Remote Sens.*, vol. 56, no. 7, pp. 4109–4125, Jul. 2018, doi: 10.1109/TGRS.2018.2826045.
- [16] D. Ho Tong Minh and Y.-N. Ngo, "Compressed SAR interferometry in the big data era," *Remote Sens.*, vol. 14, no. 2, pp. 1–13, Jan. 2022, doi: 10.3390/rs14020390. [Online]. Available: <https://www.mdpi.com/2072-4292/14/2/390>
- [17] S. Zwieback, "Cheap, valid regularizers for improved interferometric phase linking," *IEEE Geosci. Remote Sens. Lett.*, vol. 19, pp. 1–4, Aug. 2022, doi: 10.1109/LGRS.2022.3197423.
- [18] J. Biggs, T. Wright, Z. Lu, and B. Parsons, "Multi-interferogram method for measuring interseismic deformation: Denali fault, Alaska," *Geophysical J. Int.*, vol. 170, no. 3, pp. 1165–1179, Sep. 2007, doi: 10.1111/j.1365-246X.2007.03415.x.
- [19] F. De Zan, A. Parizzi, P. Prats-Iraola, and P. López-Dekker, "A SAR interferometric model for soil moisture," *IEEE Trans. Geosci. Remote Sens.*, vol. 52, no. 1, pp. 418–425, Jan. 2014, doi: 10.1109/TGRS.2013.2241069.
- [20] S. Tebaldini, F. Rocca, M. Mariotti d'Alessandro, and L. Ferro-Famil, "Phase calibration of airborne tomographic SAR data via phase center double localization," *IEEE Trans. Geosci. Remote Sens.*, vol. 54, no. 3, pp. 1775–1792, Mar. 2016, doi: 10.1109/TGRS.2015.2488358.
- [21] H. Ansari, F. De Zan, and A. Parizzi, "Study of systematic bias in measuring surface deformation with SAR interferometry," *IEEE Trans. Geosci. Remote Sens.*, vol. 59, no. 2, pp. 1285–1301, Feb. 2021, doi: 10.1109/TGRS.2020.3003421.
- [22] H. Yu, Y. Lan, Z. Yuan, J. Xu, and H. Lee, "Phase unwrapping in InSAR: A review," *IEEE Geosci. Remote Sens. Mag. (replaced Newsletter)*, vol. 7, no. 1, pp. 40–58, Mar. 2019, doi: 10.1109/MGRS.2018.2873644.
- [23] D. Ho Tong Minh, T. Le Toan, F. Rocca, S. Tebaldini, M. Mariotti d'Alessandro, and L. Villard, "Relating P-band synthetic aperture radar tomography to tropical forest biomass," *IEEE Trans. Geosci. Remote Sens.*, vol. 52, no. 2, pp. 967–979, Feb. 2014, doi: 10.1109/TGRS.2013.2246170.
- [24] A. Reigber and A. Moreira, "First demonstration of airborne SAR tomography using multibaseline L-band data," *IEEE Trans. Geosci. Remote Sens.*, vol. 38, no. 5, pp. 2142–2152, Sep. 2000, doi: 10.1109/36.868873.
- [25] S. Tebaldini, D. Ho Tong Minh, M. M. d'Alessandro, L. Villard, T. Le Toan, and J. Chave, "The status of technologies to measure forest biomass and structural properties: State of the art in SAR tomography of tropical forests," *Surv. Geophys.*, vol. 40, no. 4, pp. 779–801, May 2019, doi: 10.1007/s10712-019-09539-7.
- [26] M. Pardini, M. Tello, V. Cazcarra-Bes, K. P. Papathanassiou, and I. Hajnsek, "L- and P-band 3-D SAR reflectivity profiles versus lidar waveforms: The AfriSAR case," *IEEE J. Sel. Topics Appl. Earth Observ. Remote Sens.*, vol. 11, no. 10, pp. 1–16, Oct. 2018, doi: 10.1109/JSTARS.2018.2847033.
- [27] I. El Moussawi et al., "Monitoring tropical forest structure using SAR tomography at L- and P-band," *Remote Sens.*, vol. 11, no. 16, Aug. 2019, Art. no. 1934, doi: 10.3390/rs11161934. [Online]. Available: <https://www.mdpi.com/2072-4292/11/16/1934>
- [28] D. Ho Tong Minh, Y.-N. Ngo, and T. T. Lê, "Potential of P-band SAR tomography in forest type classification," *Remote Sens.*, vol. 13, no. 4, Feb. 2021, Art. no. 696, doi: 10.3390/rs13040696. [Online]. Available: <https://www.mdpi.com/2072-4292/13/4/696>
- [29] D. Ho Tong Minh et al., "SAR tomography for the retrieval of forest biomass and height: Cross-validation at two tropical forest sites in French Guiana," *Remote Sens. Environ.*, vol. 175, pp. 138–147, Mar. 2016, doi: 10.1016/j.rse.2015.12.037.
- [30] Y.-N. Ngo, Y. Huang, D. H. T. Minh, L. Ferro-Famil, I. Fayad, and N. Baghdadi, "Tropical forest vertical structure characterization: From GEDI to P-band SAR tomography," *IEEE Geosci. Remote Sens. Lett.*, vol. 19, pp. 1–5, Sep. 2022, doi: 10.1109/LGRS.2022.3208744.
- [31] I. El Moussawi et al., "L-band UAVSAR tomographic imaging in dense forests: Gabon forests," *Remote Sens.*, vol. 11, no. 5, Feb.

- 2019, Art. no. 475, doi: 10.3390/rs11050475. [Online]. Available: <https://www.mdpi.com/2072-4292/11/5/475>
- [32] V. Wasik, P. C. Dubois-Fernandez, C. Taillandier, and S. S. Saatchi, "The AfriSAR campaign: Tomographic analysis with phase-screen correction for P-band acquisitions," *IEEE J. Sel. Topics Appl. Earth Observ. Remote Sens.*, vol. 11, no. 10, pp. 1–13, Oct. 2018, doi: 10.1109/JSTARS.2018.2831441.
- [33] S. Tebaldini, "Algebraic synthesis of forest scenarios from multibaseline polinsar data," *IEEE Trans. Geosci. Remote Sens.*, vol. 47, no. 12, pp. 4132–4142, Dec. 2009, doi: 10.1109/TGRS.2009.2023785.
- [34] K. Goel and N. Adam, "A distributed scatterer interferometry approach for precision monitoring of known surface deformation phenomena," *IEEE Trans. Geosci. Remote Sens.*, vol. 52, no. 9, pp. 5454–5468, Sep. 2014, doi: 10.1109/TGRS.2013.2289370.
- [35] D. Ho Tong Minh, L. Van Trung, and T. L. Toan, "Mapping ground subsidence phenomena in Ho Chi Minh city through the radar interferometry technique using ALOS PALSAR data," *Remote Sens.*, vol. 7, no. 7, pp. 8543–8562, Jul. 2015, doi: 10.3390/rs70708543. [Online]. Available: <https://www.mdpi.com/2072-4292/7/7/8543>
- [36] N. Cao, H. Lee, and H. C. Jung, "A phase-decomposition-based PSInSAR processing method," *IEEE Trans. Geosci. Remote Sens.*, vol. 54, no. 2, pp. 1074–1090, Feb. 2016, doi: 10.1109/TGRS.2015.2473818.
- [37] J. Cohen-Waeber, R. Bürgmann, E. Chaussard, C. Giannico, and A. Ferretti, "Spatiotemporal patterns of precipitation-modulated landslide deformation from independent component analysis of InSAR time series," *Geophys. Res. Lett.*, vol. 45, no. 4, pp. 1878–1887, Feb. 2018, doi: 10.1002/2017GL075950. [Online]. Available: <https://agupubs.onlinelibrary.wiley.com/doi/abs/10.1002/2017GL075950>
- [38] B. Fruneau, D. Ho Tong Minh, and D. Raucoules, *Anthropogenic Activity: Monitoring Surface-Motion Consequences of Human Activities With Spaceborne InSAR*. Hoboken, NJ, USA: Wiley, 2022, ch. 1, pp. 283–313.
- [39] D. Ho Tong Minh et al., "Measuring ground subsidence in Ha Noi through the radar interferometry technique using TerraSAR-X and cosmos SkyMed data," *IEEE J. Sel. Topics Appl. Earth Observ. Remote Sens.*, vol. 12, no. 10, pp. 3874–3884, Oct. 2019, doi: 10.1109/JSTARS.2019.2937398.
- [40] M. Jiang, X. Ding, R. F. Hanssen, R. Malhotra, and L. Chang, "Fast statistically homogeneous pixel selection for covariance matrix estimation for multitemporal InSAR," *IEEE Trans. Geosci. Remote Sens.*, vol. 53, no. 3, pp. 1213–1224, Mar. 2015, doi: 10.1109/TGRS.2014.2336237.
- [41] X. Lv, B. Yazici, M. Zeghal, V. Bennett, and T. Abdoun, "Joint-scatterer processing for time-series InSAR," *IEEE Trans. Geosci. Remote Sens.*, vol. 52, no. 11, pp. 7205–7221, Nov. 2014, doi: 10.1109/TGRS.2014.2309346.
- [42] R. Shamshiri, H. Nahavandchi, M. Motagh, and A. Hooper, "Efficient ground surface displacement monitoring using Sentinel-1 data: Integrating distributed scatterers (DS) identified using two-sample t-test with persistent scatterers (PS)," *Remote Sens.*, vol. 10, no. 5, May 2018, Art. no. 794, doi: 10.3390/rs10050794. [Online]. Available: <https://www.mdpi.com/2072-4292/10/5/794>
- [43] K. Spaans and A. Hooper, "InSAR processing for volcano monitoring and other near-real time applications," *J. Geophysical Res., Solid Earth*, vol. 121, no. 4, pp. 2947–2960, Apr. 2016, doi: 10.1002/2015JB012752. [Online]. Available: <https://agupubs.onlinelibrary.wiley.com/doi/abs/10.1002/2015JB012752>
- [44] A. B. Narayan, A. Tiwari, R. Dwivedi, and O. Dikshit, "A novel measure for categorization and optimal phase history retrieval of distributed scatterers for InSAR applications," *IEEE Trans. Geosci. Remote Sens.*, vol. 56, no. 10, pp. 5843–5849, Oct. 2018, doi: 10.1109/TGRS.2018.2826842.
- [45] J. Engelbrecht and M. R. Inggs, "Coherence optimization and its limitations for deformation monitoring in dynamic agricultural environments," *IEEE J. Sel. Topics Appl. Earth Observ. Remote Sens.*, vol. 9, no. 12, pp. 5647–5654, Dec. 2016, doi: 10.1109/JSTARS.2016.2593946.
- [46] A. G. Mullissa, D. Perissin, V. A. Tolpekin, and A. Stein, "Polarimetry-based distributed scatterer processing method for PSI applications," *IEEE Trans. Geosci. Remote Sens.*, vol. 56, no. 6, pp. 3371–3382, Jun. 2018, doi: 10.1109/TGRS.2018.2798705.
- [47] G. Krieger et al., "Advanced L-band SAR system concepts for high-resolution ultra-wide-swath SAR imaging," in *Proc. ESA Adv. RF Sens. Remote Sens. Instrum. (ARSI)*, Sep. 2017. [Online]. Available: <https://elib.dlr.de/113598/>
- [48] J. Mittermayer, G. Krieger, A. Bojarski, M. Zonno, and A. Moreira, "A mirrorSAR case study based on the X-band high resolution wide swath satellite (HRWS)," in *Proc. Eur. Conf. Synthetic Aperture Radar*, 2021, pp. 1–6.
- [49] R. Torres et al., "GMES Sentinel-1 mission," *Remote Sens. Environ.*, vol. 120, pp. 9–24, May 2012, doi: 10.1016/j.rse.2011.05.028. [Online]. Available: <http://www.sciencedirect.com/science/article/pii/S0034425712000600>
- [50] P. A. Rosen, Y. Kim, R. Kumar, T. Misra, R. Bhan, and V. R. Sagi, "Global persistent SAR sampling with the NASA-ISRO SAR (NISAR) mission," in *Proc. IEEE Radar Conf. (RadarConf)*, May 2017, pp. 0410–0414, doi: 10.1109/RADAR.2017.7944237.
- [51] H. Ansari, F. De Zan, and R. Bamler, "Sequential estimator: Toward efficient InSAR time series analysis," *IEEE Trans. Geosci. Remote Sens.*, vol. 55, no. 10, pp. 5637–5652, Oct. 2017, doi: 10.1109/TGRS.2017.2711037.
- [52] I. T. Jolliffe, *Principal Component Analysis*. New York, NY, USA: Springer-Verlag, 2002.
- [53] L. R. Brigitte and H. Rouanet, *Geometric Data Analysis, From Correspondence Analysis to Structured Data Analysis*. Dordrecht, The Netherlands: Kluwer, 2004.
- [54] D. Ho Tong Minh and Y.-N. Ngo, "ComSAR: A new algorithm for processing big data SAR interferometry," in *Proc. IEEE Int. Geosci. Remote Sens. Symp. (IGARSS)*, 2021, pp. 820–823, doi: 10.1109/IGARSS47720.2021.9553675.
- [55] M. Pandey et al., "The transformational role of GPU computing and deep learning in drug discovery," *Nature Mach. Intell.*, vol. 4, no. 3, pp. 211–221, Mar. 2022, doi: 10.1038/s42256-022-00463-x.
- [56] D. Ho Tong Minh and Y.-N. Ngo, "Tomosar platform supports for Sentinel-1 tops persistent scatterers interferometry," in *Proc.*

- IEEE Int. Geosci. Remote Sens. Symp. (IGARSS)*, Jul. 2017, pp. 1680–1683, doi: 10.1109/IGARSS.2017.8127297.
- [57] Y. Xu et al., "Artificial intelligence: A powerful paradigm for scientific research," *Innovation*, vol. 2, no. 4, Nov. 2021, Art. no. 100179, doi: 10.1016/j.xinn.2021.100179. [Online]. Available: <https://www.sciencedirect.com/science/article/pii/S2666675821001041>
- [58] Y. LeCun, Y. Bengio, and G. Hinton, "Deep learning," *Nature*, vol. 521, no. 7553, pp. 436–444, May 2015, doi: 10.1038/nature14539.
- [59] R. Baraniuk, D. Donoho, and M. Gavish, "The science of deep learning," *Proc. Nat. Acad. Sci.*, vol. 117, no. 48, pp. 30,029–30,032, Nov. 2020, doi: 10.1073/pnas.2020596117. [Online]. Available: <https://www.pnas.org/doi/abs/10.1073/pnas.2020596117>
- [60] D. Ho Tong Minh et al., "Deep recurrent neural networks for winter vegetation quality mapping via multitemporal SAR Sentinel-1," *IEEE Geosci. Remote Sens. Lett.*, vol. 15, no. 3, pp. 464–468, Mar. 2018, doi: 10.1109/LGRS.2018.2794581.
- [61] D. Ienco, R. Interdonato, R. Gaetano, and D. Ho Tong Minh, "Combining Sentinel-1 and Sentinel-2 satellite image time series for land cover mapping via a multi-source deep learning architecture," *ISPRS J. Photogrammetry Remote Sens.*, vol. 158, pp. 11–22, Dec. 2019, doi: 10.1016/j.isprsjprs.2019.09.016. [Online]. Available: <https://www.sciencedirect.com/science/article/pii/S0924271619302278>
- [62] Z. Lin, K. Ji, X. Leng, and G. Kuang, "Squeeze and excitation rank faster R-CNN for ship detection in SAR images," *IEEE Geosci. Remote Sens. Lett.*, vol. 16, no. 5, pp. 751–755, May 2019, doi: 10.1109/LGRS.2018.2882551.
- [63] H. Li, F. Zhu, X. Zheng, M. Liu, and G. Chen, "MSCDUNet: A deep learning framework for built-up area change detection integrating multispectral, SAR, and VHR data," *IEEE J. Sel. Topics Appl. Earth Observ. Remote Sens.*, vol. 15, pp. 5163–5176, Jun. 2022, doi: 10.1109/JSTARS.2022.3181155.
- [64] B. Rouet-Leduc, R. Jolivet, M. Dalaison, P. A. Johnson, and C. Hulbert, "Autonomous extraction of millimeter-scale deformation in InSAR time series using deep learning," *Nature Commun.*, vol. 12, Nov. 2021, Art. no. 6480.
- [65] Y. J. E. Gbodjo, O. Montet, D. Ienco, R. Gaetano, and S. Dupuy, "Multisensor land cover classification with sparsely annotated data based on convolutional neural networks and self-distillation," *IEEE J. Sel. Topics Appl. Earth Observ. Remote Sens.*, vol. 14, pp. 11,485–11,499, Oct. 2021, doi: 10.1109/JSTARS.2021.3119191.
- [66] C. Zhang et al., "Blind super-resolution for SAR images with speckle noise based on deep learning probabilistic degradation model and SAR priors," *Remote Sens.*, vol. 15, no. 2, Jan. 2023, Art. no. 330, doi: 10.3390/rs15020330. [Online]. Available: <https://www.mdpi.com/2072-4292/15/2/330>
- [67] E. Ndikumana, D. Ho Tong Minh, N. Baghdadi, D. Courault, and L. Hossard, "Deep recurrent neural network for agricultural classification using multitemporal SAR Sentinel-1 for Camargue, France," *Remote Sens.*, vol. 10, no. 8, Aug. 2018, Art. no. 1217, doi: 10.3390/rs10081217. [Online]. Available: <https://www.mdpi.com/2072-4292/10/8/1217>
- [68] A. G. Mullissa, D. Marcos, D. Tuia, M. Herold, and J. Reiche, "deSpeckNet: Generalizing deep learning based SAR image despeckling," *IEEE Trans. Geosci. Remote Sens.*, vol. 60, pp. 1–15, 2022, doi: 10.1109/TGRS.2020.3042694.
- [69] W. Wu, H. Li, L. Zhang, X. Li, and H. Guo, "High-resolution PolSAR scene classification with pretrained deep convnets and manifold polarimetric parameters," *IEEE Trans. Geosci. Remote Sens.*, vol. 56, no. 10, pp. 6159–6168, Oct. 2018, doi: 10.1109/TGRS.2018.2833156.
- [70] Z. Wu, T. Wang, Y. Wang, R. Wang, and D. Ge, "Deep-learning-based phase discontinuity prediction for 2-D phase unwrapping of SAR interferograms," *IEEE Trans. Geosci. Remote Sens.*, vol. 60, pp. 1–16, 2022, doi: 10.1109/TGRS.2021.3121906.
- [71] L. Zhou, H. Yu, Y. Lan, and M. Xing, "Deep learning-based branch-cut method for InSAR two-dimensional phase unwrapping," *IEEE Trans. Geosci. Remote Sens.*, vol. 60, pp. 1–15, 2022, doi: 10.1109/TGRS.2021.3099997.
- [72] T. Yang, H. Yu, and Y. Wang, "Selection of persistent scatterers with a deep convolutional neural network," in *Proc. IEEE Int. Geosci. Remote Sens. Symp. (IGARSS)*, 2022, pp. 2912–2915, doi: 10.1109/IGARSS46834.2022.9884199.
- [73] L. Zhang and B. Du, "Deep learning for remote sensing data: A technical tutorial on the state of the art," *IEEE Geosci. Remote Sens. Mag. (replaced Newsletter)*, vol. 4, no. 2, pp. 22–40, Jun. 2016, doi: 10.1109/MGRS.2016.2540798.
- [74] J. A. Barrachina, Nov. 2022, "Negu93/CVNN: Complex-valued neural networks," Zenodo, doi: 10.5281/zenodo.7303587.
- [75] T. Scarnati and B. Lewis, "Complex-valued neural networks for synthetic aperture radar image classification," in *Proc. IEEE Radar Conf. (RadarConf)*, 2021, pp. 1–6, doi: 10.1109/RadarConf2147009.2021.9455316.
- [76] Y. Zhang, H. Yuan, H. Li, C. Wei, and C. Yao, "Complex-valued graph neural network on space target classification for defocused ISAR images," *IEEE Geosci. Remote Sens. Lett.*, vol. 19, pp. 1–5, Jun. 2022, doi: 10.1109/LGRS.2022.3185709.
- [77] O. Ronneberger, P. Fischer, and T. Brox, "U-Net: Convolutional networks for biomedical image segmentation," 2015. [Online]. Available: <https://arxiv.org/abs/1505.04597>
- [78] H. H. Zeyada, M. S. Mostafa, M. M. Ezz, A. H. Nasr, and H. M. Harb, "Resolving phase unwrapping in interferometric synthetic aperture radar using deep recurrent residual U-Net," *Egyptian J. Remote Sens. Space Sci.*, vol. 25, no. 1, pp. 1–10, Feb. 2022, doi: 10.1016/j.ejrs.2021.12.001. [Online]. Available: <https://www.sciencedirect.com/science/article/pii/S1110982321000958>
- [79] F. Zhou, H. Zhou, Z. Yang, and L. Gu, "IF2CNN: Towards non-stationary time series feature extraction by integrating iterative filtering and convolutional neural networks," *Expert Syst. Appl.*, vol. 170, May 2021, Art. no. 114527, doi: 10.1016/j.eswa.2020.114527. [Online]. Available: <https://www.sciencedirect.com/science/article/pii/S0957417420311714>